

---

This is an electronic reprint of the original article.  
This reprint may differ from the original in pagination and typographic detail.

Kivisaari, Pyry; Oksanen, Jani; Tulkki, Jukka

**Polarization doping and the efficiency of III-nitride optoelectronic devices**

*Published in:*  
Applied Physics Letters

*DOI:*  
[10.1063/1.4833155](https://doi.org/10.1063/1.4833155)

Published: 01/01/2013

*Document Version*  
Publisher's PDF, also known as Version of record

*Published under the following license:*  
Unspecified

*Please cite the original version:*  
Kivisaari, P., Oksanen, J., & Tulkki, J. (2013). Polarization doping and the efficiency of III-nitride optoelectronic devices. *Applied Physics Letters*, 103(21). <https://doi.org/10.1063/1.4833155>

---

This material is protected by copyright and other intellectual property rights, and duplication or sale of all or part of any of the repository collections is not permitted, except that material may be duplicated by you for your research use or educational purposes in electronic or print form. You must obtain permission for any other use. Electronic or print copies may not be offered, whether for sale or otherwise to anyone who is not an authorised user.

# Polarization doping and the efficiency of III-nitride optoelectronic devices

Cite as: Appl. Phys. Lett. **103**, 211118 (2013); <https://doi.org/10.1063/1.4833155>

Submitted: 14 March 2013 • Accepted: 07 November 2013 • Published Online: 22 November 2013

Pyry Kivisaari, Jani Oksanen and Jukka Tulkki



View Online



Export Citation



CrossMark

## ARTICLES YOU MAY BE INTERESTED IN

[Polarization doping: Reservoir effects of the substrate in AlGaIn graded layers](#)

Journal of Applied Physics **112**, 053711 (2012); <https://doi.org/10.1063/1.4750039>

[Polarization induced pn-junction without dopant in graded AlGaIn coherently strained on GaN](#)

Applied Physics Letters **101**, 122103 (2012); <https://doi.org/10.1063/1.4753993>

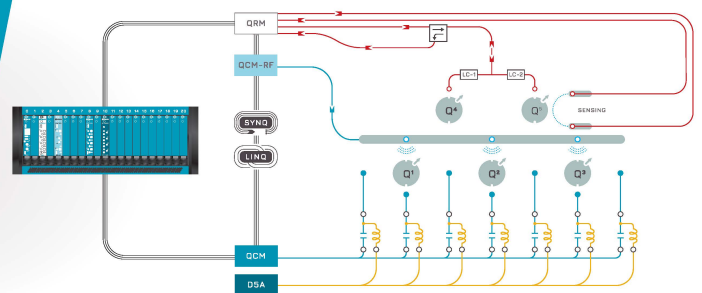
[Polarization induced hole doping in graded  \$\text{Al}\_x\text{Ga}\_{1-x}\text{N}\$  \( \$x=0.7\sim 1\$ \) layer grown by molecular beam epitaxy](#)

Applied Physics Letters **102**, 062108 (2013); <https://doi.org/10.1063/1.4792685>

 QBLOX

Integrates all  
Instrumentation + Software  
for Control and Readout of  
**Spin Qubits**

[visit our website >](#)



# Polarization doping and the efficiency of III-nitride optoelectronic devices

Pyry Kivisaari, Jani Oksanen, and Jukka Tulkki

Department of Biomedical Engineering and Computational Science, Aalto University, P.O. Box 12200, FI-00076 Aalto, Finland

(Received 14 March 2013; accepted 7 November 2013; published online 22 November 2013)

The intrinsic polarization is generally considered a nuisance in III-nitride devices, but recent studies have shown that it can be used to enhance p- and n-type conductivity and even to replace impurity doping. We show by numerical simulations that polarization-doped light-emitting diode (LED) structures have a significant performance advantage over conventional impurity-doped LED structures. Our results indicate that polarization doping decreases electric fields inside the active region and potential barriers in the depletion region, as well as the magnitude of the quantum-confined Stark effect. The simulations also predict at least an order of magnitude increase in the current density corresponding to the maximum efficiency (i.e., smaller droop) as compared to impurity-doped structures. The obtained high doping concentrations could also enable, e.g., fabrication of III-N resonant tunneling diodes and improved ohmic contacts. © 2013 AIP Publishing LLC. [<http://dx.doi.org/10.1063/1.4833155>]

High performance light-emitting diodes (LEDs) based on GaN have started a revolutionary change in the lighting industry. Despite the success, the GaN technology still faces several challenges that stand in the way of further improvements. One is the inefficient activation of Mg acceptors,<sup>1</sup> which at present is partly solved by using very large Mg densities. However, even for large Mg concentrations the conductivity remains relatively low and as an additional disadvantage, the diffusion of Mg atoms to quantum wells (QW) increases during fabrication. This reduces the quantum efficiency of light emission.<sup>2</sup>

A recently proposed method to improve the properties of p-type GaN is polarization doping. It uses the internal polarization of the structures and material composition grading to induce free electrons or holes<sup>3-7</sup> and even allows to fabricate pn junctions where free carriers are generated purely by the polarization charge without using any impurity doping.<sup>8,9</sup> Polarization doping has also been suggested, e.g., as a way to fabricate nanowire solar cells<sup>10</sup> and low-resistance ohmic contacts.<sup>11</sup>

In conventional III-N QW structures, the abrupt polarization differences between the GaN barriers and InGaN QW active regions (ARs) create large electric fields which result in the separation of electrons and holes in the QWs and decrease the recombination rate.<sup>12,13</sup> Abrupt polarization charges are also known to hinder current transport into the AR and decrease the device efficiency.<sup>14,15</sup> Polarization doping, on the other hand, enables making use of the spontaneous and piezoelectric polarization by distributing the polarization gradient in a wider region. This way polarization serves as a dopant and its deteriorating effects are expected to decrease or even disappear.

Despite experimental proof-of-concept reports on polarization doping, numerical simulations that account for the current transport in fully polarization-doped structures have not yet been reported. The goal of this work is to compare the performance of conventional impurity-doped structures to polarization-doped structures and predict the main differences in performance. We discuss the origin of polarization

doping and simulate the operation of impurity-doped and polarization-doped AlGaIn/GaN and GaN/InGaIn structures. We show that polarization doping reduces electric fields inside the AR and decreases the potential barriers in the depletion region, leading to a significantly smaller efficiency droop.

Fig. 1 shows a schematic cross-section of all the studied structures. Layer thicknesses and compositions are listed in Table I. The AlGaIn/GaN structures A and B of Table I are purely polarization-doped and have 100 nm thick graded regions around the GaN AR, mimicking the experimentally demonstrated structures of Refs. 8 and 9. The comparable conventional structures C and D with GaN QW AR have an n- and p-type AlGaIn layer below the AR, respectively, to also compare the effect of changing the electric field direction in the structure. The GaN/InGaIn structure E of Table I has polarization-doped graded regions of only 10 nm around its AR to compensate for the larger lattice mismatch. The comparable impurity-doped GaN/InGaIn QW structures F and G of Table I again have the n- and p-type layers below the QW AR, respectively. All the structures are assumed to be Ga-face grown in the [0001] direction, which is typically the case when they are grown on sapphire substrate. In this article we study the structures as simple 1D structures.

The internal polarization  $P$  of wurtzite III-N alloys consists of spontaneous and piezoelectric polarizations  $P^{sp}$  and  $P^{pz}$  as

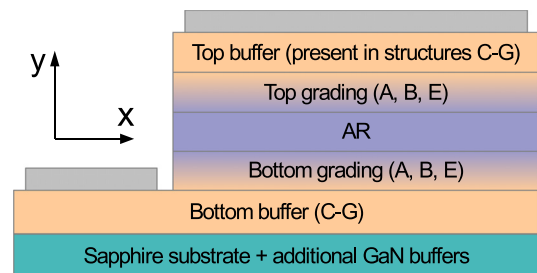


FIG. 1. Schematic cross-section of studied structures. The layer thicknesses and compositions are specified in Table I.

TABLE I. Layer thicknesses and compositions of the studied structures (refer to Fig. 1): A and B are polarization-doped  $\text{Al}_{0.3}\text{Ga}_{0.7}\text{N}/\text{GaN}$  structures, C and D are impurity-doped  $\text{Al}_{0.3}\text{Ga}_{0.7}\text{N}/\text{GaN}$  structures, E is a partly polarization-doped  $\text{GaN}/\text{In}_{0.15}\text{Ga}_{0.85}\text{N}$  structure, and F and G are impurity-doped  $\text{GaN}/\text{In}_{0.15}\text{Ga}_{0.85}\text{N}$  structures. The indicated layer thicknesses are shared by structures A-D and E-G. Note that structures B and E do not contain a well-defined QW since the necessary carrier confinement is provided by the grading.

Sample	Bottom buffer	Bottom grading	AR	Top grading	Top buffer
	100 nm	100 nm	5 nm	100 nm	100 nm
A	N/A	GaN $\rightarrow$ AlGaN	GaN	AlGaN $\rightarrow$ GaN	N/A
B	N/A	AlGaN $\rightarrow$ GaN	GaN	GaN $\rightarrow$ AlGaN	N/A
C	n-AlGaN	N/A	GaN	N/A	p-AlGaN
D	p-AlGaN	N/A	GaN	N/A	n-AlGaN
	100 nm	10 nm	5 nm	10 nm	100 nm
E	p-GaN	GaN $\rightarrow$ InGaN	InGaN	InGaN $\rightarrow$ GaN	n-GaN
F	n-GaN	N/A	InGaN	N/A	p-GaN
G	p-GaN	N/A	InGaN	N/A	n-GaN

$$P = P^{sp} + P^{pz}. \quad (1)$$

Both spontaneous and piezoelectric polarizations arise from the shift between anion and cation sublattices of the wurtzite crystal structure. Spontaneous polarization is the built-in polarization of the unstrained crystal, whereas piezoelectric polarization occurs in strained structures where atoms are displaced from their equilibrium positions. With Ga-face growth, the spontaneous polarization points in the negative direction with respect to growth direction, i.e., downward in Fig. 1. The direction of the piezoelectric polarization resulting from strain is positive for compressive strain (e.g., InGaN grown on GaN) and negative for tensile strain (e.g., AlGaN grown on GaN). If N-face growth is used instead, all the mentioned polarization directions are inverted.

All the equations needed for calculating  $P^{sp}$  and  $P^{pz}$  in AlGaN and InGaN are listed compactly in Ref. 16. However, in our calculations we multiply the polarization values given in Ref. 16 by 0.5 to account for background impurity density and composition fluctuations, as suggested in Refs. 17 and 18. Based on the equations of Ref. 16, the total polarization of a III-N material has a weakly nonlinear and monotonous dependence on the molar fraction of Al or In. Therefore, if a material is graded linearly in the  $y$  direction of Fig. 1 between two different III-N material compositions, the spatial derivative  $dP/dy$  of the polarization is approximately constant. To understand how grading results in effective doping it suffices to write the Poisson's equation as

$$\frac{d}{dy} \left( -\varepsilon \frac{d}{dy} \phi \right) = q \left( p - n + N - \frac{1}{q} \frac{dP}{dy} \right), \quad (2)$$

where  $\varepsilon$  is the permittivity,  $\phi$  is the electrostatic potential,  $q$  is the elementary charge,  $p$  is the hole density,  $n$  is the electron density,  $N$  is the ionized impurity doping density (positive for donors and negative for acceptors), and the constitutive relation  $\mathbf{D} = -\varepsilon \nabla \phi + \mathbf{P}$  has been used. Equation (2) shows that grading results in an additional charge density on the right-hand side. The generally weak nonlinear dependency of polarization makes also the polarization doping density weakly position-dependent for linear gradients.

In addition to solving Poisson's equation for our structures, we simulate current transport by solving the drift-diffusion equations. Further details and parameters of the model can be found in References 15 and 19–21. Based on Ref. 20, we use electron and hole mobilities of  $1000 \text{ cm}^2/\text{Vs}$  and  $70 \text{ cm}^2/\text{Vs}$  in GaN and calculate mobilities for the AlGaN and InGaN alloys by linear interpolation between these and the mobilities given for other binary alloys in Ref. 20. For impurity-doped p-type alloys, which typically exhibit smaller mobility, we use a hole mobility of  $5 \text{ cm}^2/\text{Vs}$ , as suggested by measurements in Ref. 21. Recombination rates are calculated in the homogeneous bulk regions and graded quasi-bulk regions (with only a gradual change in the bandgap) by using the conventional ABC model,<sup>22</sup> which accounts for the Shockley-Read-Hall (SRH) recombination with  $\tau_n, \tau_p = 1/A = 10^{-7} \text{ s}$ , net radiative recombination with  $B = 2.5 \times 10^{-17} \text{ m}^3/\text{s}$ , and Auger recombination with  $C_n, C_p = 10^{-42} \text{ m}^6/\text{s}$ . In QWs surrounded by abrupt heterointerfaces, the recombination coefficients are affected by the reduced overlap of the envelope wave functions of electrons and holes. This effect is taken into account using the approximation derived in Ref. 23, where the bulk SRH, radiative, and Auger recombination coefficients are all multiplied by the overlap factor  $|\langle \phi_c | \phi_v \rangle|^2$  of the ground state electron and hole wave functions  $\phi_c$  and  $\phi_v$  in the QWs. For simplicity, the overlap factors are calculated separately as a function of the electric fields in the QWs, and the obtained tabulated values of the overlaps are then used in the transport simulations. The emission energy of a QW is also given by the difference between the conduction and valence band ground states of the QW. If a strong electric field is present in the QW, this difference can be smaller than the bandgap of the bulk material.

By setting suitable boundary conditions, the described equation system can be solved self-consistently to get the band diagrams, electron and hole densities and currents, and local recombination rates. In calculating the net radiative recombination coefficient  $B$ , we assume that the net radiative recombination rate within the LED cavity is proportional to radiative recombination coefficient  $B_0$  (corresponding to the radiative recombination coefficient of the active region material with ideal extraction) with a proportionality factor 0.5. This factor corresponds to 1 minus the photon recycling factor, photon escape probability (from the AR), or, if optical losses outside of the AR can be neglected, to the light extraction efficiency.<sup>19,24</sup> Recombination rate densities are integrated over the volume of the whole LED to obtain the total recombination rate of the whole device, since radiative recombination in the transparent region is negligible.

Fig. 2 shows the average polarization doping density when the material is linearly graded from  $\text{Al}_{0.3}\text{Ga}_{0.7}\text{N}$  to GaN or from GaN to  $\text{In}_{0.15}\text{Ga}_{0.85}\text{N}$ . The horizontal axis shows the distance at which the grading takes place. Using these material compositions one can typically reach polarization doping densities in excess of  $10^{24} \text{ 1/m}^3$  with a grading distance of a few tens of nanometres. The predicted doping density obtained using an AlGaN  $\rightarrow$  GaN grading is in good agreement with measurements of Ref. 3, where a grading between 0% and 30% Al composition over a distance of 100 nm resulted in a free carrier density of  $1.6 \times 10^{24} \text{ 1/m}^3$ .

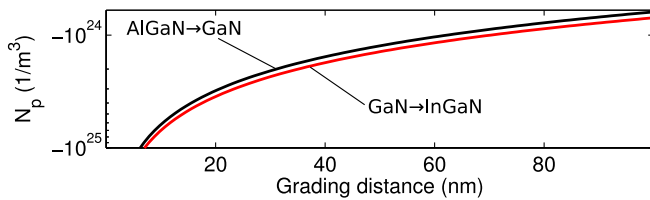


FIG. 2. Polarization-induced p-type doping densities as a function of the distance at which the material is graded from  $\text{Al}_{0.3}\text{Ga}_{0.7}\text{N}$  to GaN or GaN to  $\text{In}_{0.15}\text{Ga}_{0.85}\text{N}$  (with Ga-face growth). If the direction of the grading changes or the growth is performed N-face, the sign of the polarization doping changes and results in n-type doping.

Note that in Fig. 2 and structures B, C, and D, the buffer is unstrained AlGaN and the GaN is strained. Structure A, on the other hand, is grown on unstrained GaN.

Left panel of Fig. 3 shows band diagrams of the AlGaN/GaN structures A-D at zero bias voltage, with the AR marked with a gray background. The band diagram of structure A in Fig. 3(a) is qualitatively similar to that reported in Ref. 8, where the grading was of the same type but in a nanowire and with a larger fraction of Al. Like in Ref. 8, there is an abrupt material and polarization change in the AlGaN-GaN interfaces of structure A leading to a large electric field in the AR. In contrast, structure B of Fig. 3(b) has no abrupt interfaces and, more importantly, no potential barriers or additional electric fields because the polarization charge is distributed over a large distance of several tens of nanometres. Structures C and D of Figs. 3(c) and 3(d) are conventional impurity-doped structures with reversed doping profiles. Due to the inverted doping profile and polarization charge densities in the AR interfaces, structure D especially has a very large electric field in the AR, which decreases the electron and hole overlap and the energy difference between conduction and valence band states.

Right panel of Fig. 3 shows the band diagrams of structures A-D at operating points that will be shown to correspond to their maximum internal quantum efficiencies

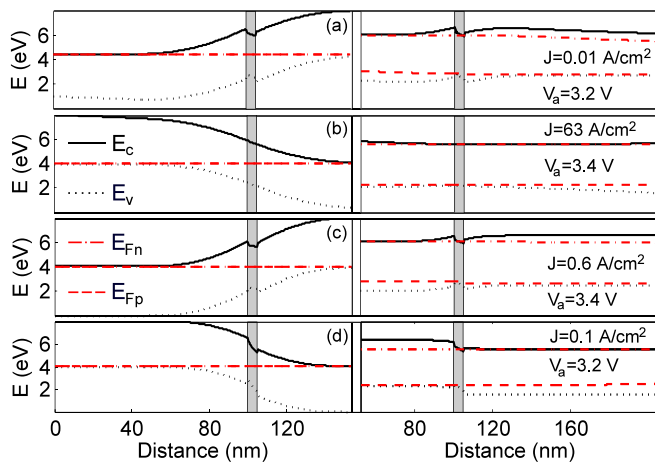


FIG. 3. Band diagram of structure (a) A, (b) B, (c) C, and (d) D at zero bias voltage (left panel) and at the operating point where the maximum IQE takes place (right panel). Note that in (b) and (d) the n- and p-type regions are on different sides than in (a) and (c).  $E_c$  is the conduction band edge,  $E_v$  is the valence band edge,  $E_{Fn}$  is the conduction band quasi-Fermi level, and  $E_{Fp}$  is the valence band quasi-Fermi level. The voltage and current density are written in the figures, and the 5 nm thick AR is marked with a gray background.

(IQEs). The applied voltages and current densities are marked in the figures. The band diagrams of (a), (c), and (d) all have large polarization-induced electric fields and surface charge densities in the AR, which result in a substantial electron-hole separation. This decreases significantly the recombination coefficients and also the current at which the peak IQE is reached. Also the band diagrams of (a) and (c) show small quasi-Fermi level changes near the AR interfaces due to polarization-induced potential barriers, and these changes become more pronounced at higher input powers. These changes slightly increase the forward voltage needed to reach a desired current density to the AR. Structure B of Fig. 3(b) has no quasi-Fermi level changes and no additional surface charges or electric fields near its AR, which is expected to increase its recombination rate as compared to the other structures. Note that we have used the standard quasi-Fermi level boundary conditions that result in the large abrupt change in minority carrier quasi-Fermi level right next to the contact. The IV characteristics of all the structures are diode-like and therefore in qualitative agreement with experimentally reported results.<sup>8,9,13</sup>

Fig. 4 shows the band diagrams of the GaN/InGaN structures E, F, and G. Band diagrams of the impurity-doped GaN/InGaN structures F and G follow the same trends as samples C and D, respectively. Most of structure E of Fig. 4(a) is impurity-doped, but the inset shows the region which includes the 10 nm thick grading from GaN to InGaN, the 5 nm thick InGaN AR, and the 10 nm thick grading from InGaN back to GaN. Both left (unbiased) and right (biased at 2.6 V) panels of Fig. 4(a) show that the 10 nm thick grading is sufficient to remove the abrupt material interfaces. The electric field in the AR is also significantly smaller in sample E than in samples F-G.

Electric field in a QW causes the electron (hole) ground state wave function to be centered near the minimum (maximum) of the conduction (valence) band edge in the QW and also makes the emission wavelength dependent on the electric field. This is a result of the quantum-confined Stark effect (QCSE, see, e.g., Ref. 26). Fig. 5(a) shows the QCSE for structures A, C, D, F, and G that all have a QW AR. Dashed lines in (a) show the bulk bandgap of the QW

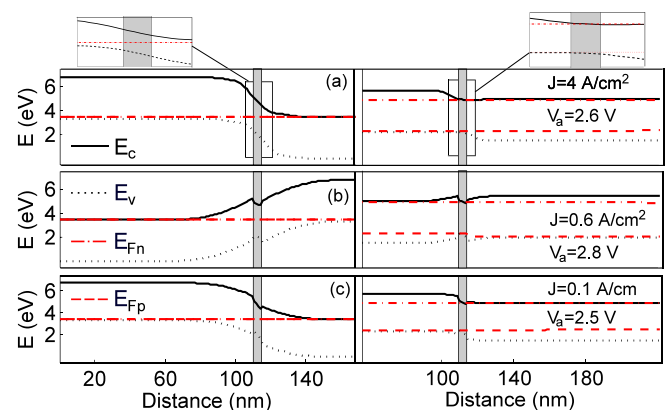


FIG. 4. Band diagram of structure (a) E, (b) F, and (c) G of Table I at zero bias voltage (left panel) and at the bias voltage where the maximum IQE takes place (right panel). Inset in (a) shows the region with the grading from GaN to InGaN, the InGaN AR, and the grading back from InGaN to GaN with no impurities.

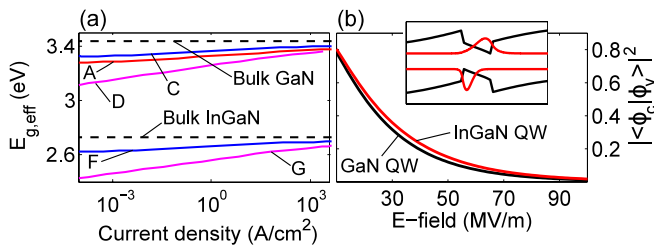


FIG. 5. (a) Effective bandgaps (i.e., energy differences between the ground states of electrons and holes) in the structures with QW ARs as a function of current density. The dependence of the effective bandgap on the input current reproduces a typical QCSE for III-N QW devices.<sup>26</sup> (b) Overlap factor  $|\langle\phi_c|\phi_v\rangle|^2$  in GaN and InGaN QWs as a function of the electric field in the QW. The inset in (b) shows the electron and hole wavefunctions together with the band edges in structure C at its maximum IQE.

material compositions. For the large electric fields of the polar QWs, the energy separation of electron and hole ground states and correspondingly the emission energy becomes smaller than the bulk bandgap. The behaviour in Fig. 5(a) is qualitatively similar to QCSE in III-N MQW devices.<sup>26</sup> Fig. 5(b) shows the squared overlap factors  $|\langle\phi_c|\phi_v\rangle|^2$  calculated for the GaN and InGaN QWs as a function of the electric field in the QW. The recombination parameters in the QW structures are considerably smaller than in the bulk due to the small overlap factors. This also significantly decreases the current density at which the IQE has its maximum. The overlaps are in a good agreement with values reported in Ref. 27. Based on the simulations, the electric fields in samples with QW AR range from 10 MV/m at high injection currents to slightly over 100 MV/m at very low injection currents. Inset in Fig. 5(b) shows an example of the electron and hole wave functions together with the band edges for structure C at its peak IQE, where  $|\langle\phi_c|\phi_v\rangle|^2 \approx 0.1$ .

IQEs of structures A-D are shown in Fig. 6(a). IQE is calculated by dividing the total radiative recombination rate obtained for radiative recombination coefficient  $B_0$  by the injection rate  $I/q$  ( $I$  being the injection current), in accordance with Ref. 28. Structure B has the highest injection current corresponding to the maximum IQE due to the absence of polarization-induced field in the AR and the resulting larger recombination rate. In structures A, C, and D, the large electric field inside the QWs significantly increases the electron hole separation in the AR. This decreases the recombination rates and leads to a small input current corresponding to the peak IQE. We define the onset of the efficiency droop as the operating point where IQE starts to decline as current increases. Therefore small droop corresponds to a high current density at the onset of the droop. Structure B has a

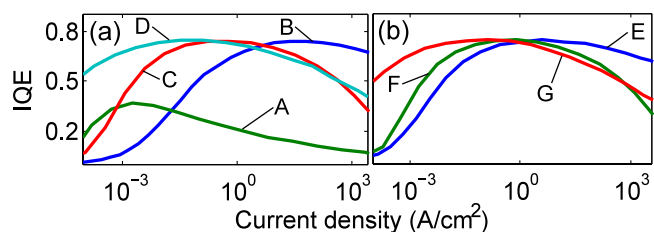


FIG. 6. IQE of (a) structures A-D and (b) structures E-G of Table I. Polarization-doped structures B and E have a significantly larger injection current corresponding to their peak IQE than their impurity-doped counterparts.

significantly smaller droop than the impurity-doped samples C and D, where the IQE peaks at small currents due to the reduced envelope wave function overlap and the strong localization of electrons and holes in the opposite sides of the QWs. The current density corresponding to the maximum IQE is  $63 \text{ A/cm}^2$  in the polarization-doped structure B, whereas in impurity-doped structure C (D) it is more than two orders of magnitude lower, namely  $0.6 \text{ A/cm}^2$  ( $0.1 \text{ A/cm}^2$ ). The IQE of the polarization-doped structure A is not essentially different from impurity-doped structures C and D, since it still features a QW with large electric field and electron-hole separation. The low IQE of structure A is caused by a large leakage current, which is favored by the linear gradients of band edges in the graded regions of Fig. 3(a).

Fig. 6(b) shows the IQEs of the GaN/InGaN structures E-G of Table I. The partly polarization-doped structure E has a smaller droop than its completely impurity-doped counterparts F-G. This is again because structures F and G have a reduced electron-hole wave function overlap, leading to reduced recombination rates for a given input voltage. The droop in the conventional structures F-G is qualitatively similar to droop in typical experimentally reported impurity-doped GaN/InGaN LEDs (see, e.g., Refs. 13, 25, and 29).

In realistic structures, the background ionized impurity density is expected to somewhat diminish the polarization hole doping.<sup>5,8</sup> Our results, however, show that even reduced polarization values result in very large doping densities and many other benefits in terms of efficiency. Also because in polarization-doped samples B and E, a small part of the radiative recombination takes place in the graded region close to the AR, polarization doping might enable a small increase in the emitting volume of the LED and slightly shift the peak IQE to higher currents.<sup>30</sup> Due to the possibility to obtain extremely high free carrier densities by polarization doping, it may also enable fabrication of, e.g., resonant tunneling diodes and improved ohmic contacts relying on carrier tunneling.

In conclusion, we studied the origin of polarization doping and compared the performance of conventional impurity-doped LED structures and structures making use of polarization doping by numerical simulations. The simulations clearly show that, as compared to impurity doping, polarization doping provides significant benefits to the operation of III-N LEDs in the form of high p-type doping and more than one order of magnitude higher current density corresponding to the maximum efficiency. Smaller droop is reached mainly due to the smaller electric fields in the light-emitting AR, leading to smaller electron-hole separation and increased recombination rates for a given carrier density. In conventional impurity-doped III-N LED structures, the intrinsic polarization is a significant disadvantage, but with polarization doping it can be fully exploited for doping in the ideal case.

The research has been supported by Aalto Energy Efficiency Research Programme (AEF) and the Academy of Finland.

<sup>1</sup>W.-C. Ke, S.-J. Lee, S.-L. Chen, C.-Y. Kao, and W.-C. Hwang, *Mater. Chem. Phys.* **133**, 1029 (2012).

<sup>2</sup>K. Köhler, T. Stephan, A. Perona, J. Wiegert, M. Maier, M. Kunzer, and J. Wagner, *J. Appl. Phys.* **97**, 104914 (2005).

- <sup>3</sup>J. Simon, A. (Kejia) Wang, H. Xing, S. Rajan, and D. Jena, *Appl. Phys. Lett.* **88**, 042109 (2006).
- <sup>4</sup>L. Zhang, K. Ding, J. C. Yan, J. X. Wang, Y. P. Zeng, T. B. Wei, Y. Y. Li, B. J. Sun, R. F. Duan, and J. M. Li, *Appl. Phys. Lett.* **97**, 062103 (2010).
- <sup>5</sup>J. Simon, V. Protasenko, C. Lian, H. Xing, and D. Jena, *Science* **327**, 60 (2010).
- <sup>6</sup>S. Li, M. E. Ware, J. Wu, V. P. Kunets, M. Hawkrige, P. Minor, Z. Wang, Z. Wu, Y. Jiang, and G. J. Salamo, *J. Appl. Phys.* **112**, 053711 (2012).
- <sup>7</sup>S. Li, T. Zhang, J. Wu, Y. Yang, Z. Wang, Z. Wu, Z. Chen, and Y. Jiang, *Appl. Phys. Lett.* **102**, 062108 (2013).
- <sup>8</sup>S. D. Carnevale, T. F. Kent, P. J. Phillips, M. J. Mills, S. Rajan, and R. C. Myers, *Nano Lett.* **12**, 915 (2012).
- <sup>9</sup>S. Li, M. Ware, J. Wu, P. Minor, Z. Wang, Z. Wu, Y. Jiang, and G. J. Salamo, *Appl. Phys. Lett.* **101**, 122103 (2012).
- <sup>10</sup>F. Boxberg, N. Sondergaard, and H. Q. Xu, *Nano Lett.* **10**, 1108 (2010).
- <sup>11</sup>M. Singh, Y. Zhang, J. Singh, and U. Mishra, *Appl. Phys. Lett.* **77**, 1867 (2000).
- <sup>12</sup>V. Fiorentini, F. Bernardini, F. Della Sala, A. Di Carlo, and P. Lugli, *Phys. Rev. B* **60**, 8849 (1999).
- <sup>13</sup>J. Xu, M. F. Schubert, A. N. Noemaun, D. Zhu, J. K. Kim, E. F. Schubert, M. H. Kim, H. J. Chung, S. Yoon, C. Sone, and Y. Park, *Appl. Phys. Lett.* **94**, 011113 (2009).
- <sup>14</sup>Y. Kawaguchi, C.-Y. Huang, Y.-R. Wu, Q. Yan, C.-C. Pan, Y. Zhao, S. Tanaka, K. Fujito, D. Feezell, C. G. Van de Walle, S. P. DenBaars, and S. Nakamura, *Appl. Phys. Lett.* **100**, 231110 (2012).
- <sup>15</sup>P. Kivisaari, J. Oksanen, and J. Tulkki, *J. Appl. Phys.* **111**, 103120 (2012).
- <sup>16</sup>V. Fiorentini, F. Bernardini, and O. Ambacher, *Appl. Phys. Lett.* **80**, 1204 (2002).
- <sup>17</sup>Y.-K. Kuo, S.-H. Horng, S.-H. Yen, M.-C. Tsai, and M.-F. Huang, *Appl. Phys. A* **98**, 509 (2010).
- <sup>18</sup>J. Piprek and S. Li, *Opt. Quantum Electron.* **42**, 89 (2010).
- <sup>19</sup>O. Heikkilä, J. Oksanen, and J. Tulkki, *J. Appl. Phys.* **107**, 033105 (2010).
- <sup>20</sup>E. Bellotti and F. Bertazzi, in *Nitride Semiconductor Devices*, edited by J. Piprek (Wiley-VCH, Weinheim, 2007), Chap. 4.
- <sup>21</sup>M. Zhang, P. Bhattacharya, W. Guo, and A. Banerjee, *Appl. Phys. Lett.* **96**, 132103 (2010).
- <sup>22</sup>S. L. Chuang, *Physics of Photonic Devices* (John Wiley & Sons, Hoboken, NJ, 2009), Ch. 2.3.
- <sup>23</sup>E. Kioupakis, Q. Yan, and C. G. Van de Walle, *Appl. Phys. Lett.* **101**, 231107 (2012).
- <sup>24</sup>J.-B. Wang, D. Ding, S. R. Johnson, S.-Q. Yu, and Y.-H. Zhang, *Phys. Status Solidi B* **244**, 2740 (2007).
- <sup>25</sup>G.-B. Lin, D. Meyaard, J. Cho, E. Fred Schubert, H. Shim, and C. Sone, *Appl. Phys. Lett.* **100**, 161106 (2012).
- <sup>26</sup>J.-H. Ryou, W. Lee, J. Limb, D. Yoo, J. P. Liu, R. D. Dupuis, Z. H. Wu, A. M. Fischer, and F. A. Ponce, *Appl. Phys. Lett.* **92**, 101113 (2008).
- <sup>27</sup>R. A. Arif, Y.-K. Ee, and N. Tansu, *Appl. Phys. Lett.* **91**, 091110 (2007).
- <sup>28</sup>E. Matioli and C. Weisbuch, in *III-Nitride Based Light Emitting Diodes and Applications*, edited by T.-Y. Seong, J. Han, H. Amano, and H. Morkoc (Springer, Dordrecht, 2013), Ch. 6.
- <sup>29</sup>P. Kivisaari, L. Riuttanen, J. Oksanen, S. Suihkonen, M. Ali, H. Lipsanen, and J. Tulkki, *Appl. Phys. Lett.* **101**, 021113 (2012).
- <sup>30</sup>A. Laubsch, M. Sabathil, J. Baur, M. Peter, and B. Hahn, *IEEE Trans. Electron Devices* **57**, 79 (2010).